Supplementary Material for

# Towards understanding the mechanisms of new particle formation in the Eastern Mediterranean

Rima Baalbaki[1], Michael Pikridas[2], Tuija Jokinen[1], Tiia Laurila[1], Lubna Dada[1], Spyros Bezantakos[2], Lauri Ahonen[1], Kimmo Neitola[1,2], Anne Maisser[2], Elie Bimenyimana[2], Aliki Christodoulou[2,3], Florin Unga[2], Chrysanthos Savvides[4], Katrianne Lehtipalo[1,5], Juha Kangasluoma[1], George Biskos[2], Tuukka Petäjä[1], Veli-Matti Kerminen[1], Jean Sciare[2], Markku Kulmala[1]

[1]Institute for Atmospheric and Earth System Research (INAR) / Physics, Faculty of Science, University of Helsinki, P.O. Box 64, Helsinki, 00014, Finland
[2]Climate & Atmosphere Research Centre (CARE-C), The Cyprus Institute, P.O. Box 27456, Nicosia, CY-1645, Cyprus
[3]IMT Lille Douai, Université de Lille, SAGE - Département Sciences de L'Atmosphère et Génie de L'Environnement, 59000, Lille, France
[4]Ministry of Labour, Welfare and Social Insurance, Department of Labour Inspection (DLI), Nicosia, Cyprus
[5]Finnish Meteorological Institute, Helsinki, Finland

*Correspondence to: rima.baalbaki@helsinki.fi*

## 1. Data availability

Table S1. Availability of hourly data (%) from the three particle measuring instruments.

| Month | PSM | NAIS | SMPS |
|---|---|---|---|
| January | 72.8 | 93.4 | 16.1 |
| February | 96.4 | 94.5 | 94.6 |
| March | 83.6 | 96.4 | 75.1 |
| April | 83.3 | 100.0 | 99.7 |
| May | 67.6 | 99.7 | 91.5 |
| June | 43.5 | 100.0 | 55.7 |
| July | 41.5 | 100.0 | 81.0 |
| August | 77.4 | 100.0 | 96.1 |
| September | 93.5 | 99.9 | 98.5 |
| October | 90.3 | 100.0 | 96.8 |
| November | 80.0 | 99.9 | 1.7 |
| December | 100.0 | 100.0 | 0.0 |

## 2. PSM setup, operation and data handling

### 2.1. PSM core sampling inlet

The PSM inlet design was first introduced by Kangasluoma et al. (2016). It is a simple design encompassing a 6-mm tube fitted inside a 10-mm tube using a Swagelok T piece (Figure S1). In normal operating conditions, the 3rd outlet of the T-piece is connected to vacuum which enables drawing higher flow through the 10-mm tube than the PSM flow, allowing the PSM to sample from the middle of this flow and thus minimizing losses caused by diffusion to the inlet walls (Figure S1a). During the background measurements, the 3rd outlet is connected to particle-free pressurized air with a high enough flow rate allowing the PSM to sample this particle free air (Figure S1b)

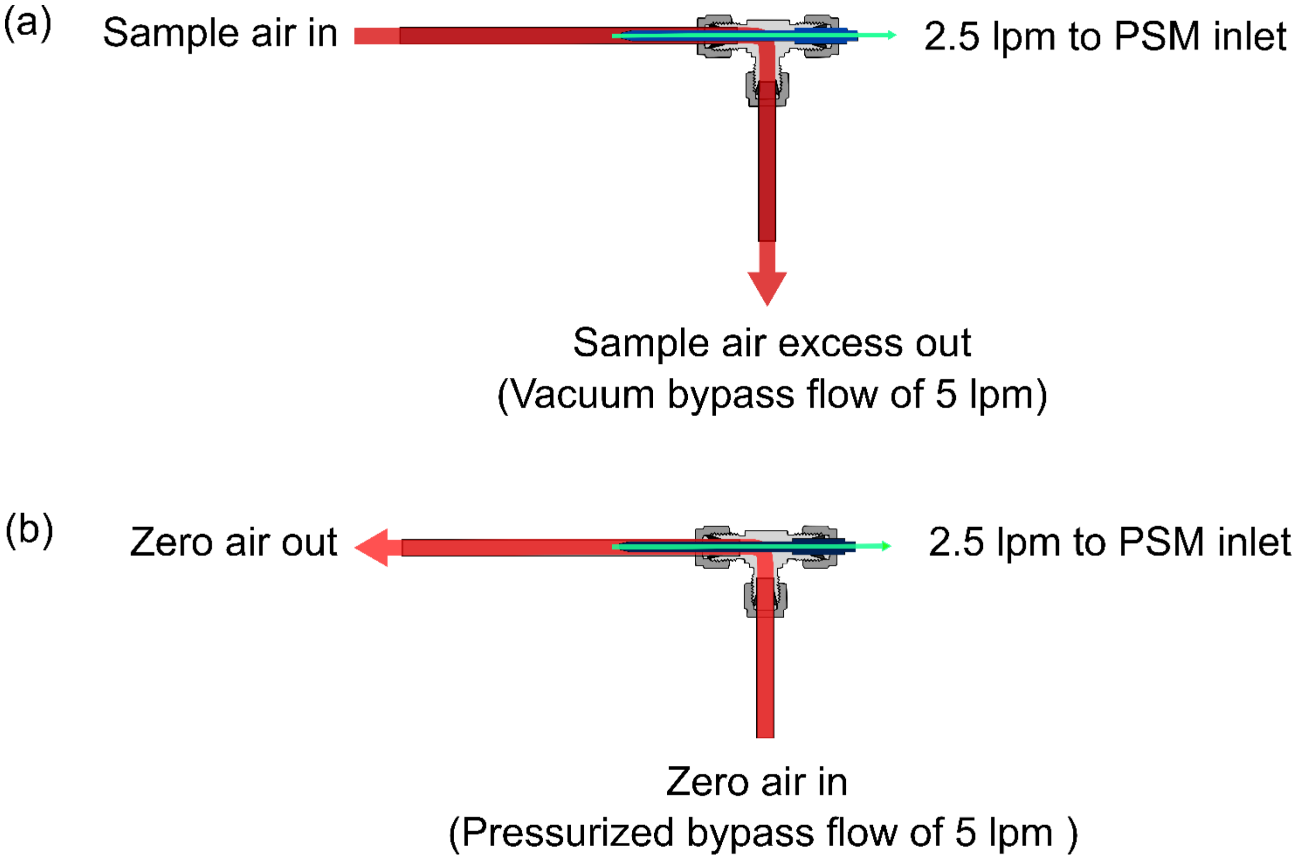


Figure S1. A schematic of the PSM core sampling inlet during normal operation (a) and during background measurements (b).

### 2.2. PSM diluter

We used a prototype diluter which was designed at the University of Helsinki and later commercialized by Airmodus under the name “Airmodus nanoparticle diluter” (AND). The diluter has a cylindrical shape made of three modules. The first module, from the air-sampling side, serves as a switchable ion filter which removes charged ions and particles up to a certain size and allows the measurement of neutral particles only. In this study the ion filter was turned off. The second module is a core sampling piece radially connected to a vacuum source which draws 5 lpm excess flow from the sampling air. The third module constitutes the dilution module where clean dry air is introduced radially into the sampled air flow. The differential pressure across the dilution unit is continuously monitored and is kept constant by a feedback mechanism to a PID controlled proportional valve which determines the dilution flow required to keep the dilution ratio constant. The design of the diluter was made as compact as possible to reduce losses and optimize penetration efficiency. Additionally, the dilution flow was monitored with a TSI flow meter and was used along with the pressure measurements to determine and correct for the real-time dilution factor.

### 2.3. nCNC (PSM+CPC) inversion

In principle, the PSM is a mixing-type condensation particle counter but without the measuring optics. It uses diethylene glycol (DEG) to grow nano-sized particles (~1-3 nm) up to around 90 nm. Subsequently, these particles enter the CPC and are further grown with butanol to sizes measurable by the CPC optical detector. In the first stage, the mixing ratio of DEG vapour with sample flow is scanned by continuously incrementing then decrementing the saturator flow between 0.1 and 1.3 liters per minute (lpm) while keeping the sample flow constant. By varying the mixing ratio, the particle cut-off size is changed (i.e., at higher mixing ratio, smaller particles are activated and grown thus lower cut-off is achieved). Therefore, the nCNC measures the total particle concentration above a certain diameter and inversion algorithms are required to retrieve the size distribution below 3 nm. The two most popular methods to invert PSM data are the kernel function method and the step inversion method. The expectation-maximization (EM) method has been recently recommended over the kernel method because it is less sensitive to random errors (Cai et al., 2018;Chan et al., 2020). Here, we compare the kernel method and the EM method using PSM data from the whole measurement period. Data pretreatment before inversion was done similarly for the two methods and included a:

1) Diagnostic check that identifies and removes erroneous data based on instrument diagnostics and flags.
2) Background subtraction: the instrumental background of the PSM was continuously monitored with daily automated random background (zero) checks. The background was subtracted from the measured data except in the cases were the background was very high (> 10% of the measured concentrations) then the corresponding data was deemed unusable until the background decreased to normal levels.
3) Correction for the time-delay between PSM and CPC which is typically ~5 seconds.
4) Noise filtering procedure achieved by applying a $6^{th}$ order median filter on the one second resolution data.
5) Quality check using the method suggested by Chan et al. (2020).
6) Minimization of the inversion matrix using a saturator flow inversion window of 0.08 lpm which minimized the saturator flow (corresponding to cut-off diameter) scans from ~120 to 16 per one-direction of the scan.
7) While pre-averaging before the inversion step is recommended for noisy data, here we did not pre-average in order to capture the fast variations in the data.
8) The minimized cut-offs matrix is differentiated to retrieve the concentration in each size bin which is the input for the kernel inversion method. This step is not necessary for the EM method which takes the cut-off matrix as input (the varying total particle concentration at each saturator flow rate). Further explanation about the theoretical approach of each inversion method can be found in Cai et al. (2018).

During the inversion step, four kernels corresponding to four size channels (dp), with the following diameters: 1.1 nm, 1.3nm, 1.5 nm, and 2.4 nm were used with the kernel inversion method whereas 50 kernels between 1.1 nm and 2.4 nm were used for the EM inversion method. The kernels are Gaussian-shaped and represent the derivative of the laboratory-derived detection efficiency curves with respect to the saturator flow rate. The median (μ) of the kernel function at each dp is equal to the saturator flow having half maximum detection efficiency at this diameter, whereas the width i.e. standard deviation (σ) is equal to $p_1/(d_p+q_1)$ where $p_1$ and $q_1$ are fitting parameters derived from the calibration curve. An example of PSM calibration curve data is shown in Figure 1 from Cai et al. (2018). Note that the actual input to the EM method is the detection efficiency curves rather than the kernels.

After the inversion step, inverted data was transformed from $dN/dd_P$ to $dN/d\log d_P$ and averaged to longer times: five minutes and one hour. The comparison of the inversion methods was made by comparing the total $dN/d\log d_P$ concentration from the kernel and EM methods to each other. The two methods were reasonably comparable using the one hour resolution data (Figure S2), although there is some scatter at low total concentrations, and the 5 min average data revealed sometimes considerable deviations. Here, we mainly use 1 hour resolution data for the presented analysis thus we chose to use the data from the kernel inversion method because it gave better uniformity for the particle size distribution below 3 nm.

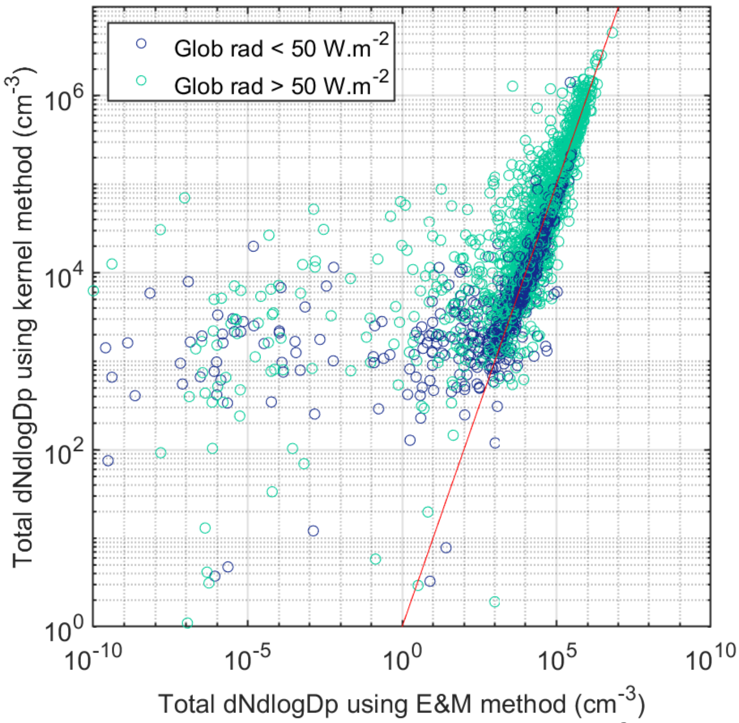


Figure S2. Comparison between total dN/dlogDp concentrations (cm$^{-3}$) between 1.1 and 2.4 nm computed from PSM data using the Kernel inversion method and the E&M method. Each data point represents one hour time resolution. Blue points represent data with global radiation lower than 50 W.m$^{-2}$ (night-time data). Green points represent data with global radiation higher than 50 W.m$^{-2}$ (day-time data). The red line represents the 1:1 line.

## 3. NAIS inlet penetration efficiency

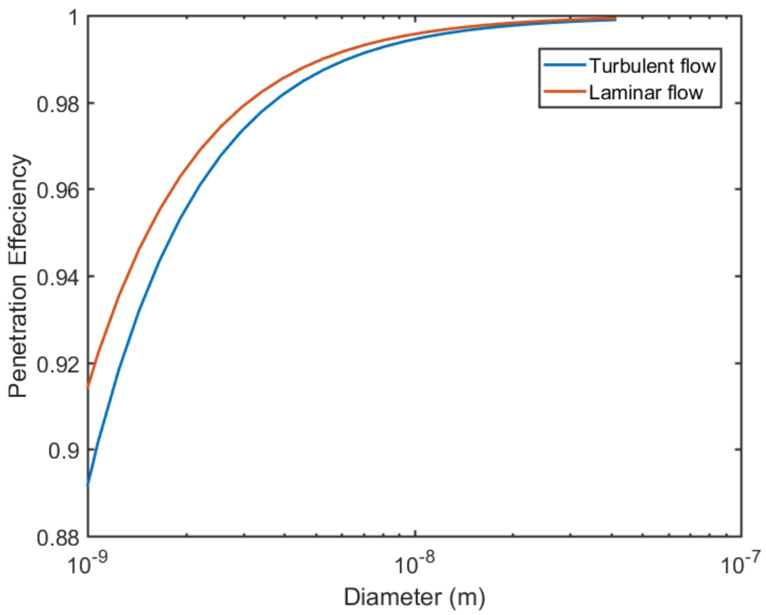


Figure S3. Penetration efficiency through the NAIS inlet based on a turbulent or laminar flow calculations.

## 4. SMPS hygroscopicity corrections

The “ambient” SMPS particle size distribution was back calculated from the dry distribution using the hygroscopicity model of Petters and Kreidenweis (2007). This model relies on the Köhler theory which describes the equilibrium between the droplet phase and vapor phase. The traditional Köhler equation (Eq. S1) links the equilibrium size of the growing aerosol particle, its chemical composition and water content to the ambient water vapor saturation ratio (S) (Köhler, 1936).

$$S = \frac{P_{w,eq}}{P_{w,sat}} = \frac{RH(D)}{100} = a_w \exp\left(\frac{4\sigma M_w}{RT\rho_w D}\right) \qquad Eq. S1$$

Where:

- $P_{w,eq}$ *is the equilibrium vapor pressure of water over the droplet surface* $(Pa)$
- $P_{w,sat}$ *is the saturation vapor pressure over a pure flat water surface* $(Pa)$
- $a_w$ *is the activity of water in solution* $(unitless)$
- $M_w$ *is the molecular weight of water* $(kg.mol^{-1})$
- $\sigma$ *is the surface tension of the solution* $-$ *air interface* $(\mathrm{N}.m^{-1})$
- $\rho_w$ *is the density of water* $(kg.m^{-3})$
- $D$ *is the diameter of the droplet* $(m)$

Petters and Kreidenweis (2007) introduced a single hygroscopicity parameter $(\kappa)$ which described the water activity $(a_w)$ and the difference in the densities and molar masses of water and the dry material:

$$\frac{1}{a_w} = 1 + \kappa \frac{V_{dry}}{V_w} \qquad Eq. S2$$

Where :

- $V_{dry}$ *is the volume of the dry aerosol particle*
- $V_w$ *is the volume of water*

Assuming additive volumes, the Köhler equation can be reformulated to the $\kappa$-Köhler equation which can also written in the form of hygroscopic growth factor (HGF) which is defined as the ratio between wet particle diameter $(D_{p,wet})$ and dry particle diameter $(D_{p,dry})$:

$$\frac{RH(D)}{100} = \frac{{D_{p,wet}}^3 - D_{p,dry}^3}{{D_{p,wet}}^3 - D_{p,dry}^3(1-\kappa)} \exp\left(\frac{4\sigma M_w}{RT\rho_w D_{p,wet}}\right) \qquad Eq. S3$$

In this study average seasonal values of $\kappa$ were retrieved from hygroscopic tandem differential mobility analyzer (HTDMA) measurements performed in parallel to our study (Table S2). The hygroscopic κ values for each SMPS size bin were extrapolated from the HTDMA size resolved measurements by linear regression. The particle size distributions at ambient RH conditions was then calculated using equation S3, by incorporating the respective κ values per size bin, and the measured size distribution at dry conditions.

Next, the ambient (real) particle diameter was calculated from $\kappa$ by solving equation S3, which was later used to calculate the real particle size distribution (before drying).

To show an example of the effect of humidity corrected particle size distribution on NPF-related parameters, we compared the dry condensation sink to that calculated when the particle sizes were assumed to be equilibrated to the ambient RH. This comparison shows that the actual condensation sink is sometimes up to 3.5 times higher than the dry condensation sink but on average it is between 1.1 and 1.3 times higher than the dry one (Figure S4).

Table S2. HTDMA derived kappa ($\kappa$) parameter.

| | HTDMA derived Kappa | | | | |
|---|---|---|---|---|---|
| Diameter (nm) | Spring | Summer | Fall | Winter | Average |
| 30 | 0.19 | 0.23 | 0.14 | 0.16 | 0.18 |
| 80 | 0.19 | 0.28 | 0.17 | 0.15 | 0.2 |
| 160 | 0.22 | 0.26 | 0.21 | 0.22 | 0.23 |

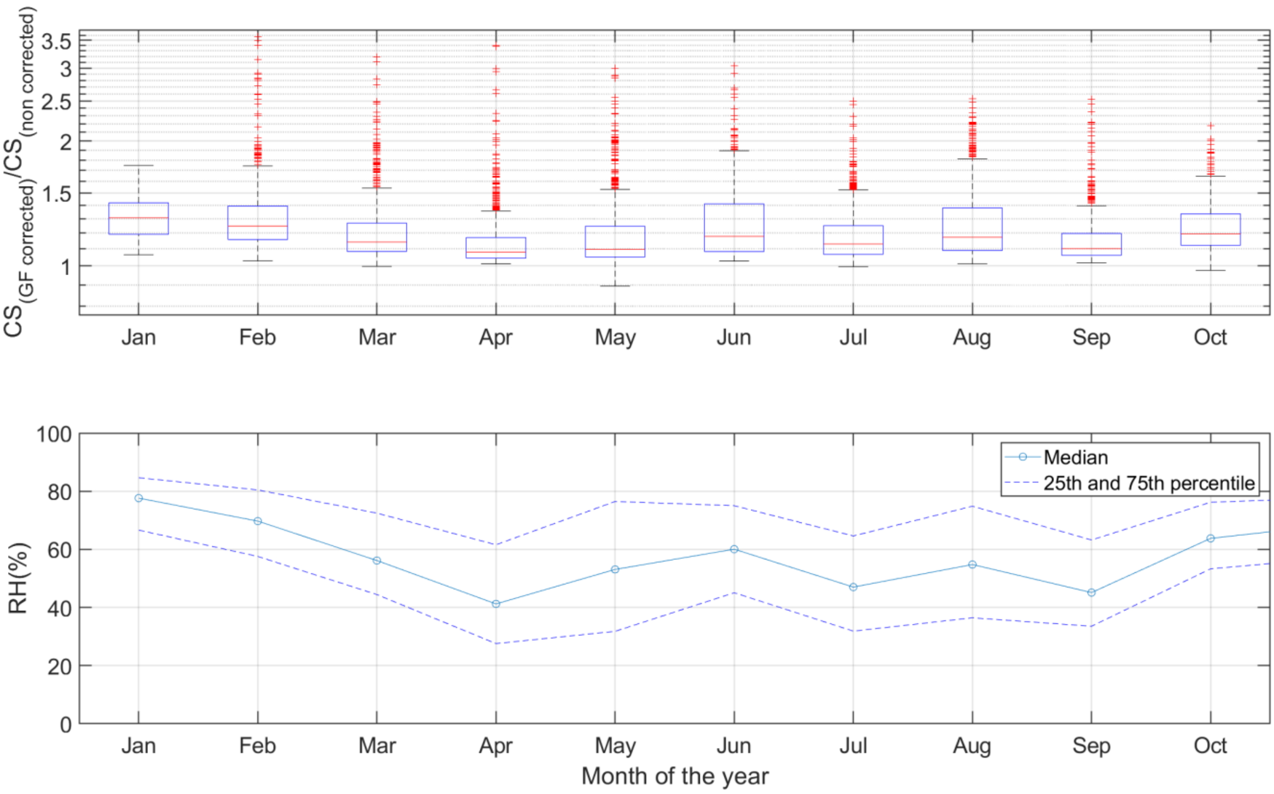


Figure S4. The top panel shows the effect of particle hygroscopic growth factor (GF) on condensation sink (CS) calculations presented as the ratio between condensation sink calculated from the "ambient" distribution and condensation sink calculated from the "dry" distribution. The bottom and top edges of the box plot represent 25% and 75% percentiles. The whiskers extend to the most extreme data points not considered outliers, and the outliers are plotted individually using the '+' symbol. The bottom panel shows median RH (%) with $25^{th}$ and $75^{th}$ percentiles.

## 5. Identification of days with high dust loading

The method proposed by Drinovec et al. (2020) permits the calculation mineral dust concentrations with high time resolution using the following equation

$$Mineral\ dust_{PM_{10-1}} = \frac{b_{abs,VI} - b_{abs,PM_1}}{EF \times MAC} \qquad Eq.S4$$

Where $b_{abs,VI}$ is the absorption coefficient (at 370nm) measured by the aethalometer (model AE33, Magee Scientific, USA) coupled to a virtual impactor (VI), $b_{abs,PM_1}$ is the absorption coefficient (at 370nm) measured by a second AE33 Aethalometer sampling through a $PM_1$ sharp-cut cyclone, EF is the enhancement factor of the VI and MAC is the mass absorption cross section for dust. The last two coefficients were used as determined experimentally by Drinovec et al. (2020) where additional information about the method and the instruments used can be found.

From the mineral dust daily time series we defined a daily threshold above which a day is considered having high dust loading (Table S3). When aethalometer measurements were not available, coarse particle mass loading ($PM_{10}$ - $PM_{2.5}$), determined by a Tapered Element Oscillating Microbalance (TEOM), was used to identify dust days. Additional information about the TEOM used can be found in Pikridas et al. (2018). The threshold for coarse PM was defined based on the linear regression between coarse PM and mineral dust concentration.

Table S3. List of dates with high dust loading

| | | | | |
|---|---|---|---|---|
| 6-Feb-18 | 21-Mar-18 | 26-Apr-18 | 22-May-18 | 23-Oct-18 |
| 7-Feb-18 | 22-Mar-18 | 27-Apr-18 | 23-May-18 | 24-Oct-18 |
| 8-Feb-18 | 23-Mar-18 | 1-May-18 | 24-May-18 | 31-Oct-18 |
| 9-Feb-18 | 24-Mar-18 | 2-May-18 | 8-Jun-18 | 1-Nov-18 |
| 10-Feb-18 | 25-Mar-18 | 3-May-18 | 9-Jun-18 | 2-Nov-18 |
| 5-Mar-18 | 26-Mar-18 | 4-May-18 | 23-Jul-18 | 3-Nov-18 |
| 6-Mar-18 | 27-Mar-18 | 5-May-18 | 24-Jul-18 | 4-Nov-18 |
| 7-Mar-18 | 28-Mar-18 | 6-May-18 | 18-Oct-18 | 24-Jan-19 |
| 8-Mar-18 | 19-Apr-18 | 7-May-18 | 19-Oct-18 | 25-Jan-19 |
| 20-Mar-18 | 20-Apr-18 | 21-May-18 | 21-Oct-18 | 26-Jan-19 |

**6. Time range of Daytime conditions (**global radiation > 50 W $m^{-2}$)

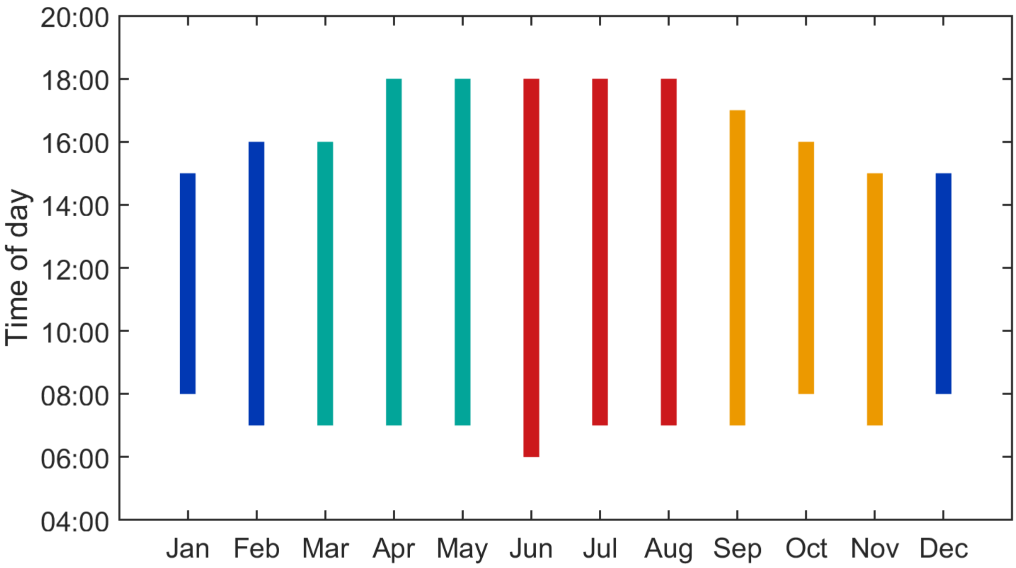


Figure S5. Monthly range of time of day having global radiation > 50 W. $m^{-2}$.

## 7. Diurnal cycle of particle mode concentrations

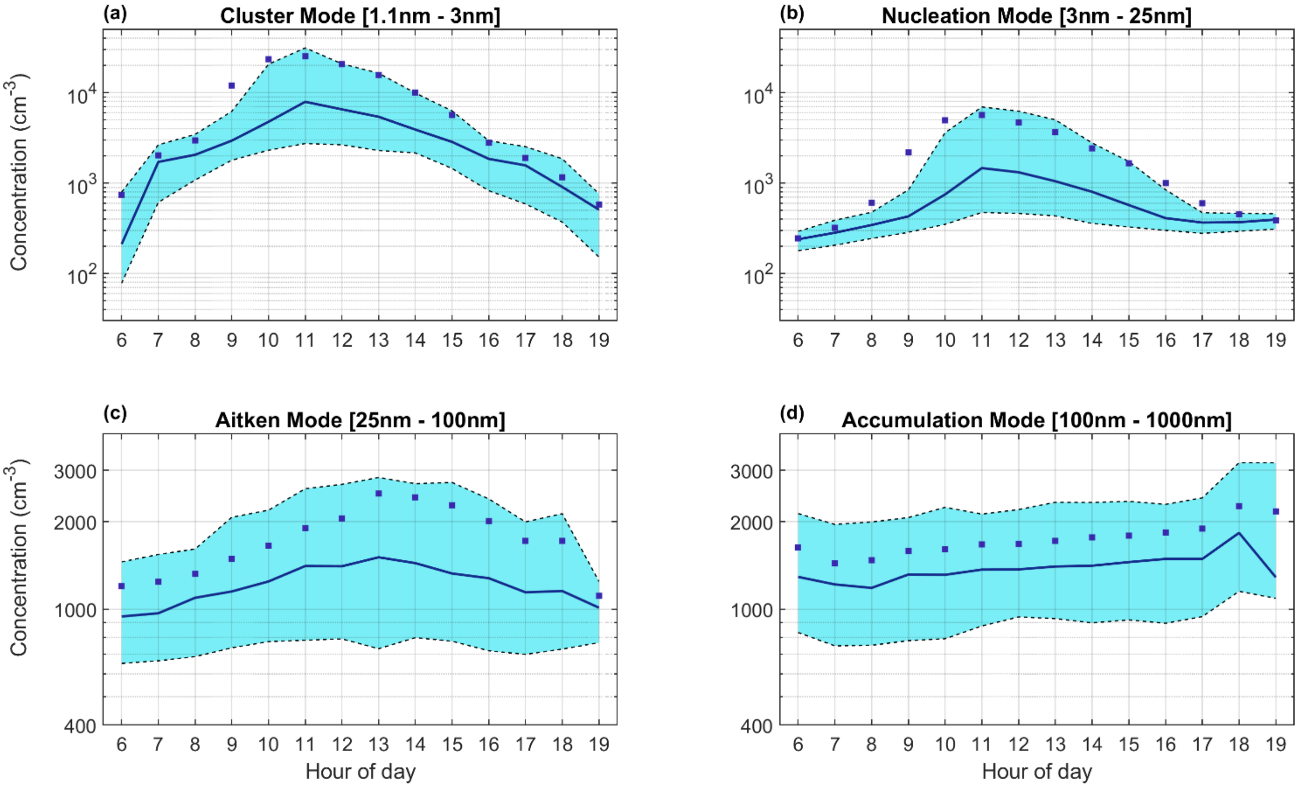


Figure S6. The diurnal cycle (at radiation >50 W. m$^{-2}$) of particle number concentration of Cluster mode (a), Nucleation mode (b), Aitken mode (c), and Accumulation mode (d). The shaded areas with black dashed boundaries represent the 25$^{th}$ and 75$^{th}$ percentile limits while the solid line represents the median and the squares indicate the mean. Notice the difference in the y-scale between the top and bottom plots.

166 ## 8. Example of event classes

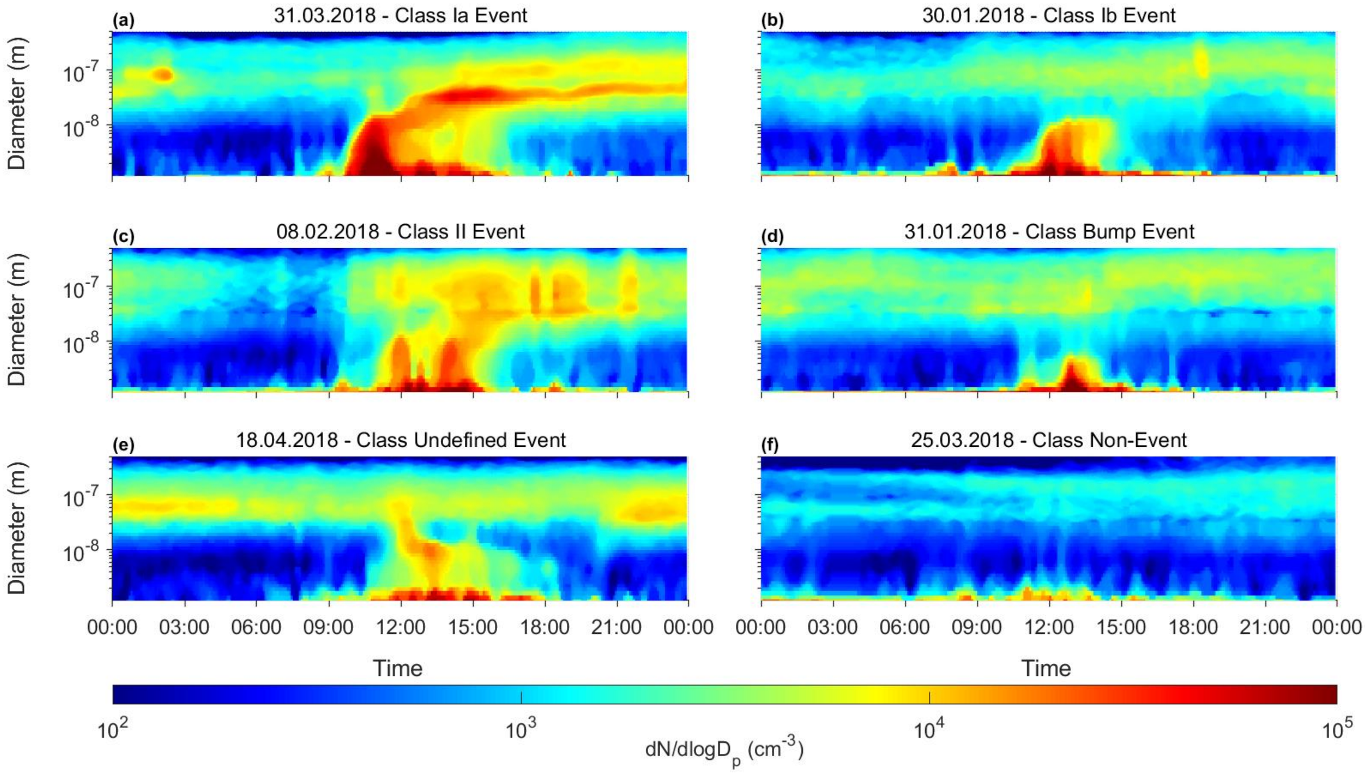


167 Figure S7. Examples of class Ia (a), class Ib (b), class II (c), bump (d), undefined (e) and non-events (f).

## 9. NPF specific parameters

Table S4. Monthly values of observed formation rates ($cm^{-3}\ s^{-1}$) during NPF events calculated within the event duration using hourly data.

| | | Jan | Feb | Mar | Apr | May | Jun | Jul | Aug | Sep | Oct | Nov | Dec | All |
|---|---|---|---|---|---|---|---|---|---|---|---|---|---|---|
| $J_{1.5}$ ($cm^{-3}\ s^{-1}$) | Mean | 11.03 | 21.74 | 26.18 | 42.23 | 8.95 | | 4.99 | 11.01 | 11.95 | 5.69 | 7.70 | | 20.34 |
| | SD | 19.43 | 41.37 | 43.77 | 93.81 | 11.24 | | 5.88 | 15.55 | 17.03 | 7.12 | 3.82 | | 51.11 |
| | 25th | 2.32 | 2.92 | 3.54 | 4.37 | 2.80 | | 0.90 | 1.90 | 1.20 | 0.71 | 4.77 | | 2.24 |
| | Median | 4.90 | 10.31 | 10.01 | 10.12 | 4.48 | | 2.14 | 4.22 | 6.70 | 3.15 | 8.15 | | 6.45 |
| | 75th | 9.47 | 23.11 | 31.40 | 41.29 | 9.74 | | 7.20 | 12.60 | 17.49 | 7.57 | 10.64 | | 18.41 |
| | 90th | 30.01 | 50.89 | 70.69 | 108.72 | 24.61 | | 14.44 | 30.82 | 24.32 | 17.53 | 11.66 | | 49.84 |
| | N | 28 | 84 | 140 | 150 | 91 | | 31 | 33 | 60 | 108 | 4 | | 729 |
| $J_3$ ($cm^{-3}\ s^{-1}$) | Mean | 2.73 | 5.52 | 8.13 | 9.72 | 4.48 | 4.45 | 5.91 | 3.89 | 6.06 | 2.51 | 2.77 | | 6.17 |
| | SD | 4.17 | 5.91 | 10.99 | 17.18 | 5.84 | 6.26 | 9.95 | 5.49 | 8.55 | 4.81 | 1.97 | | 10.65 |
| | 25th | 0.45 | 1.46 | 1.60 | 1.55 | 0.81 | 0.76 | 0.53 | 0.46 | 0.36 | 0.28 | 1.45 | | 0.79 |
| | Median | 1.65 | 3.81 | 3.62 | 3.85 | 2.03 | 1.46 | 2.46 | 1.08 | 2.15 | 0.63 | 2.42 | | 2.53 |
| | 75th | 2.55 | 7.51 | 9.99 | 11.00 | 5.64 | 6.35 | 5.47 | 6.13 | 8.54 | 2.19 | 4.09 | | 6.82 |
| | 90th | 7.35 | 14.27 | 20.18 | 23.77 | 10.59 | 11.21 | 19.81 | 12.75 | 17.38 | 6.69 | 5.45 | | 16.91 |
| | N | 28 | 83 | 134 | 166 | 109 | 31 | 47 | 36 | 60 | 96 | 4 | | 794 |
| $J_7$ ($cm^{-3}\ s^{-1}$) | Mean | 0.79 | 1.81 | 1.57 | 1.73 | 1.75 | 0.55 | 2.13 | 0.69 | 1.37 | 0.79 | 1.01 | | 1.47 |
| | SD | 0.87 | 2.02 | 1.75 | 2.83 | 2.11 | 0.57 | 4.43 | 1.16 | 2.05 | 0.79 | 0.43 | | 2.26 |
| | 25th | 0.21 | 0.46 | 0.31 | 0.30 | 0.20 | 0.20 | 0.10 | 0.08 | 0.21 | 0.17 | 0.70 | | 0.22 |
| | Median | 0.46 | 1.38 | 0.94 | 0.67 | 1.04 | 0.37 | 0.49 | 0.23 | 0.61 | 0.53 | 1.15 | | 0.65 |
| | 75th | 1.21 | 2.31 | 2.23 | 2.12 | 2.19 | 0.76 | 1.79 | 0.77 | 1.64 | 1.33 | 1.33 | | 1.86 |
| | 90th | 2.07 | 3.88 | 4.02 | 4.04 | 5.35 | 1.25 | 6.90 | 2.40 | 3.41 | 2.03 | 1.35 | | 3.81 |
| | N | 26 | 83 | 130 | 163 | 103 | 31 | 49 | 37 | 57 | 93 | 4 | | 776 |

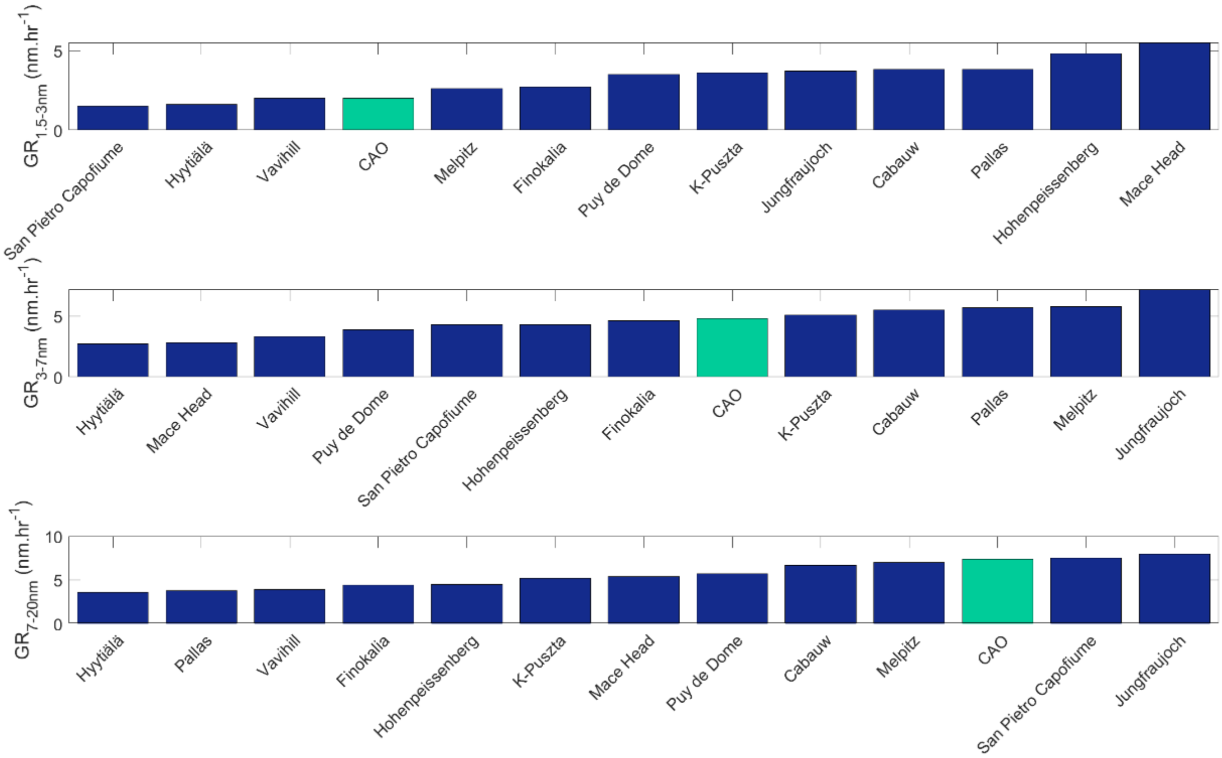


Figure S8. Comparison of growth rates measured in this study to growth rates measured at 12 European sites (Manninen et al., 2010).

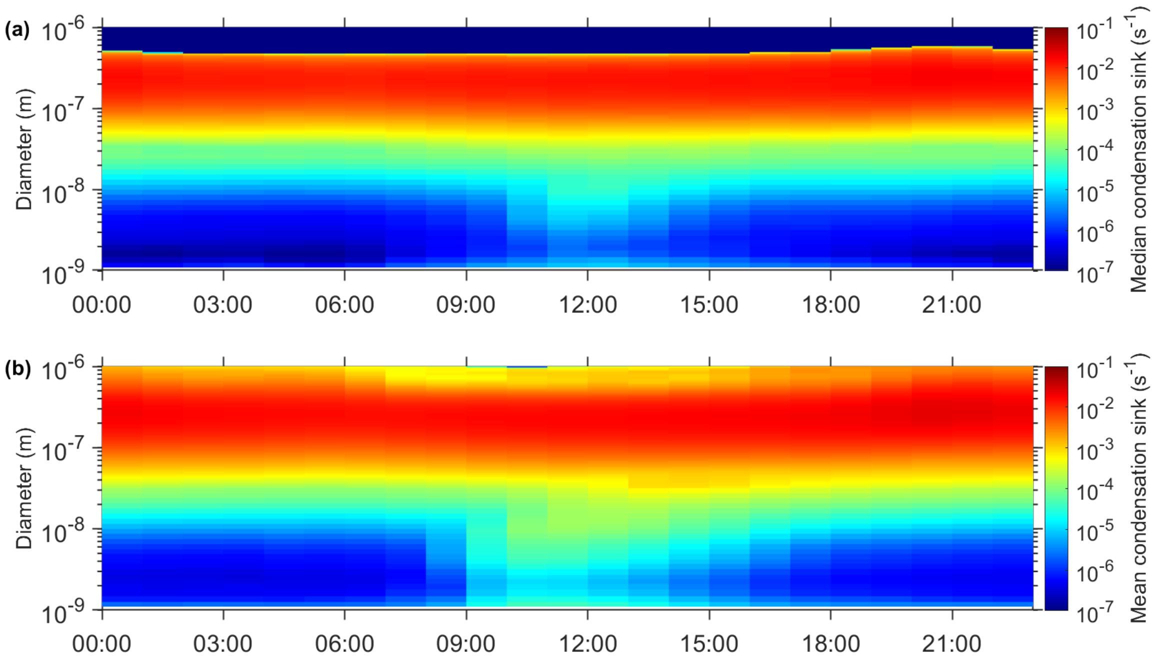


Figure S9. The median (a) and mean (b) averages of the diurnal size segregated condensation sink ($s^{-1}$) computed over the whole measurement period of this study.

Table S5. Seasonal comparison between condensation sink ($\times10^{-3}$ $s^{-1}$) measured at Finokalia, Crete and CAO (Mean, Median and Standard deviation computed from daily medians).

| | Finokalia Kalivitis et al. (2019) | | | CAO This Study | | |
|---|---|---|---|---|---|---|
| | Mean | Median | SD | Mean | Median | SD |
| Winter | 4.3 | 3.5 | 2.9 | 12.18 | 9.11 | 8.35 |
| Spring | 5.8 | 5.5 | 3.0 | 14.07 | 12.97 | 7.86 |
| Summer | 9.1 | 9.0 | 3.1 | 10.65 | 7.84 | 9.39 |
| Autumn | 6.5 | 6.0 | 3.4 | 5.16 | 4.97 | 2.15 |

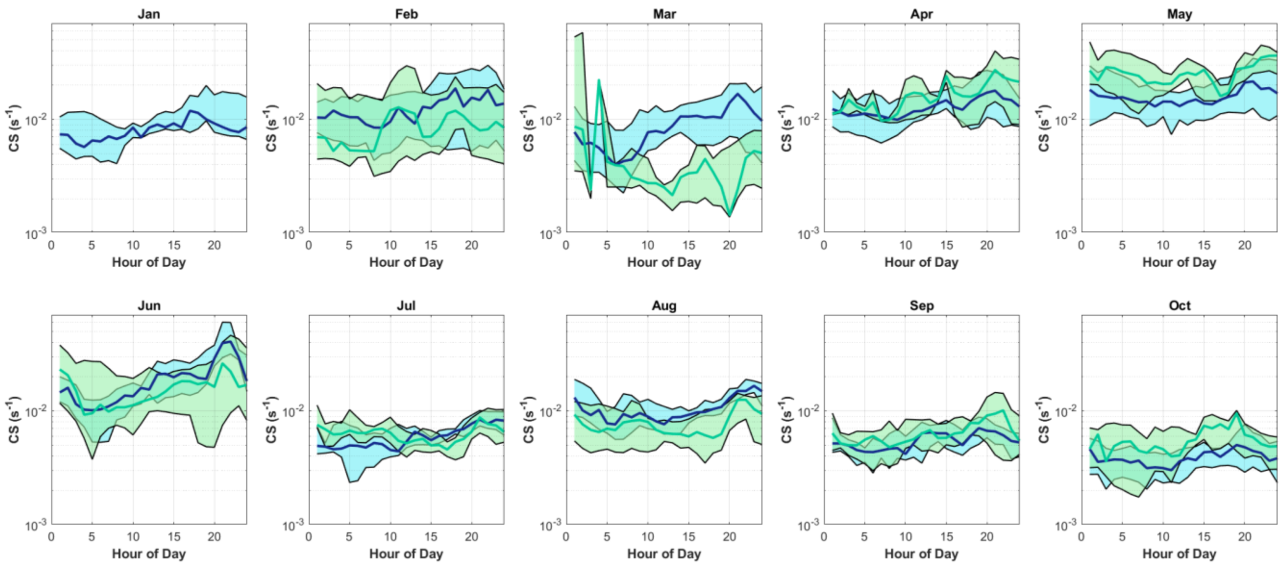


Figure S10. The monthly diurnal cycle of condensation sink ($s^{-1}$) during event (blue) and non-event (green) days. The shaded areas represent 25th to 75th percentile while the solid line represents the median.

## 10. The relation between some parameters and NPF events

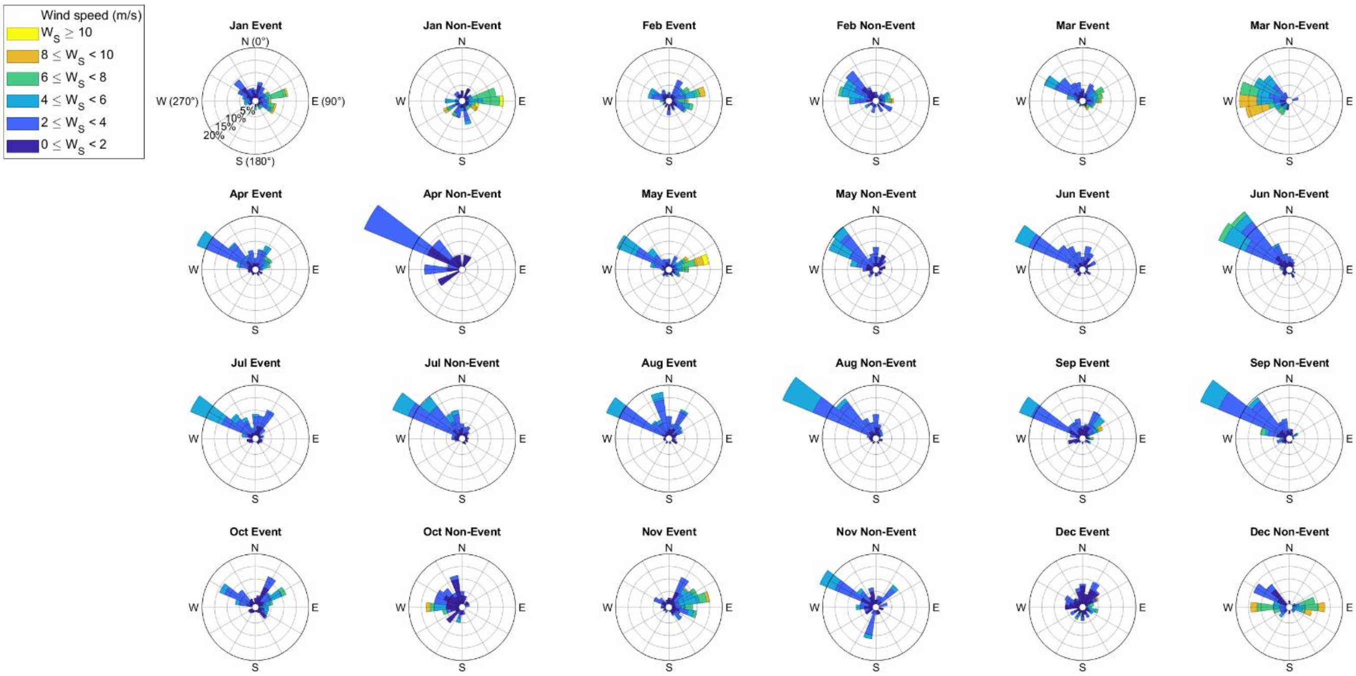


Figure S11. Month wind roses during event and non-event days.

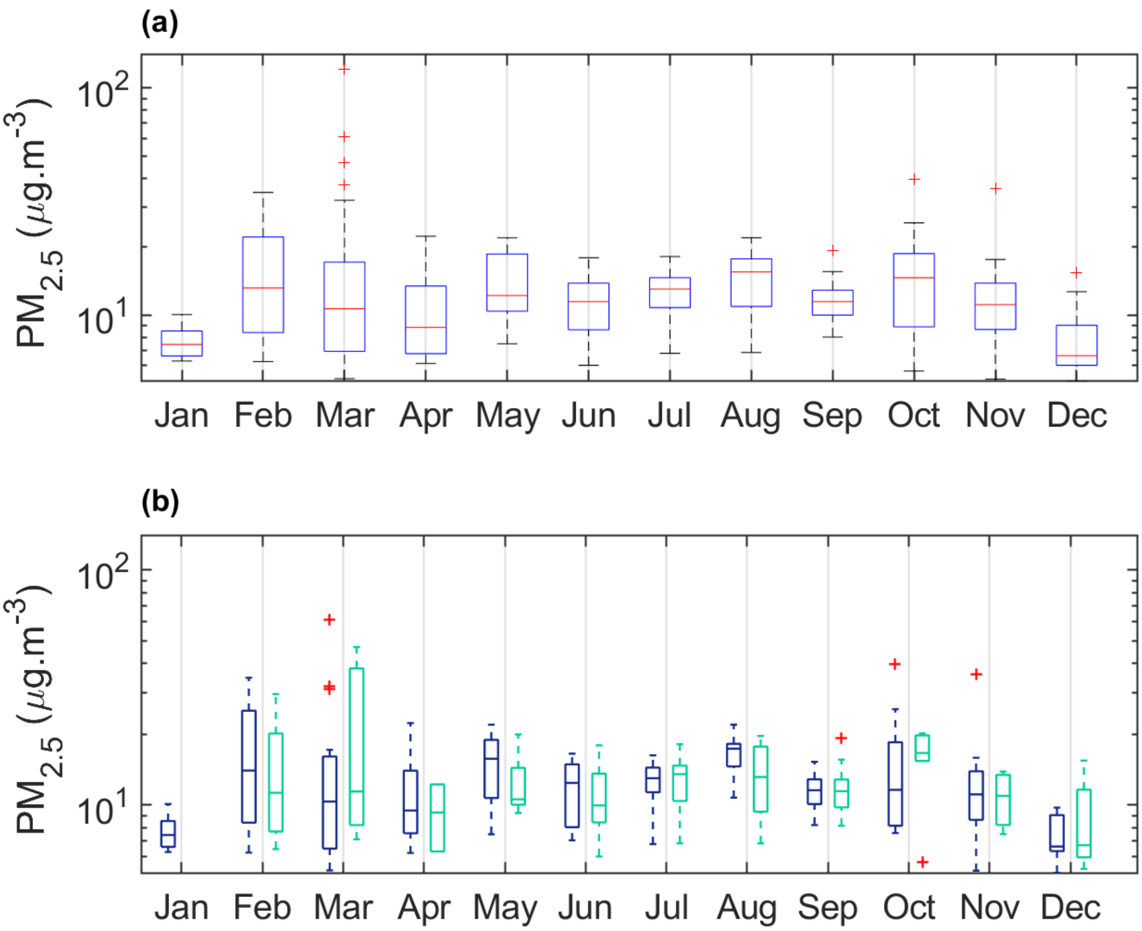


Figure S12. (a) Monthly variation of $PM_{2.5}$ (µg.m$^{-3}$). (b) Monthly variation of $PM_{2.5}$ (µg.m$^{-3}$) separated between event (blue) and non-event (green) days. The bottom and top edges of the box plots indicate the 25$^{th}$ and 75$^{th}$ percentiles, respectively. The central mark indicates the median. The whiskers extend to the most extreme data points not considered outliers, and the outliers are plotted individually using the '+' symbol. Data presented have daily time resolution.

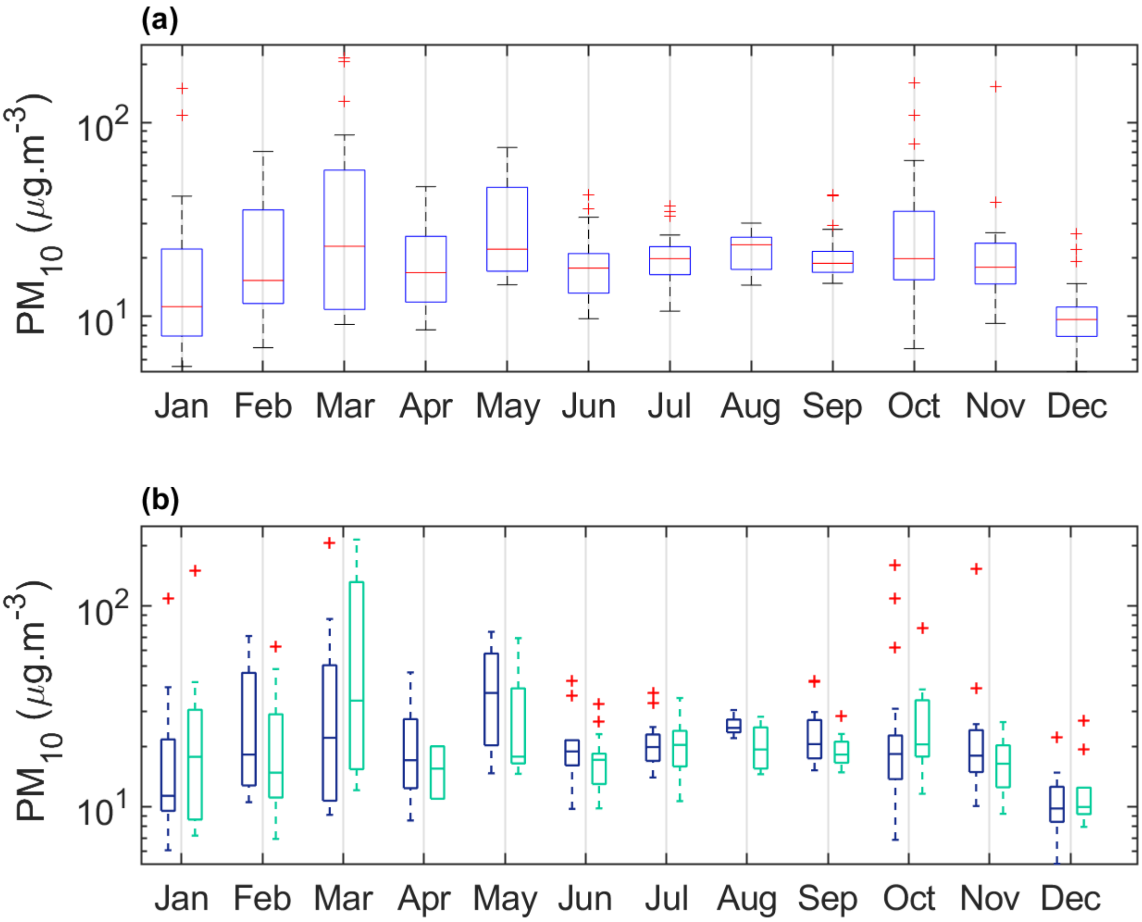


Figure S13. (a) Monthly variation of $PM_{10}$ ($\mu g.m^{-3}$). (b) Monthly variation of $PM_{10}$ ($\mu g.m^{-3}$) separated between event (blue) and non-event (green) days. The bottom and top edges of the box plots indicate the $25^{th}$ and $75^{th}$ percentiles, respectively. The central mark indicates the median. The whiskers extend to the most extreme data points not considered outliers, and the outliers are plotted individually using the '+' symbol. Data presented have daily time resolution

## References


Cai, R., Yang, D., Ahonen, L. R., Shi, L., Korhonen, F., Ma, Y., Hao, J., Petäjä, T., Zheng, J., Kangasluoma, J., and Jiang, J.: Data inversion methods to determine sub-3 nm aerosol size distributions using the particle size magnifier, Atmospheric Measurement Techniques, 11, 4477-4491, https://doi.org/10.5194/amt-11-4477-2018, 2018.

Chan, T., Cai, R., Ahonen, L. R., Liu, Y., Zhou, Y., Vanhanen, J., Dada, L., Chao, Y., Liu, Y., Wang, L., Kulmala, M., and Kangasluoma, J.: Assessment of particle size magnifier inversion methods to obtain particle size distribution from atmospheric measurements, Atmospheric measurement Techniques Discussions, 2020, 1-21, https://doi.org/10.5194/amt-2019-465, 2020.

Drinovec, L., Sciare, J., Stavroulas, I., Bezantakos, S., Pikridas, M., Unga, F., Savvides, C., Višić, B., Remškar, M., and Močnik, G.: A new optical-based technique for real-time measurements of mineral dust concentration in PM10 using a virtual impactor, Atmospheric Measurement Techniques, 13, 3799-3813, https://doi.org/10.5194/amt-13-3799-2020, 2020.

Kalivitis, N., Kerminen, V. M., Kouvarakis, G., Stavroulas, I., Tzitzikalaki, E., Kalkavouras, P., Daskalakis, N., Myriokefalitakis, S., Bougiatioti, A., Manninen, H. E., Roldin, P., Petäjä, T., Boy, M., Kulmala, M., Kanakidou, M., and Mihalopoulos, N.: Formation and growth of atmospheric nanoparticles in the eastern Mediterranean: results from long-term measurements and process simulations, Atmospheric Chemistry and Physics, 19, 2671-2686, https://doi.org/10.5194/acp-19-2671-2019, 2019.

Kangasluoma, J., Franchin, A., Duplissy, J., Ahonen, L., Korhonen, F., Attoui, M., Mikkilä, J., Lehtipalo, K., Vanhanen, J., Kulmala, M., and Petäjä, T.: Operation of the Airmodus A11 nano Condensation Nucleus Counter at various inlet pressures and various operation temperatures, and design of a new inlet system, Atmospheric Measurement Techniques, 9, 2977-2988, https://doi.org/10.5194/amt-9-2977-2016, 2016.

Köhler, H.: The nucleus in and the growth of hygroscopic droplets, Transactions of the Faraday Society, 32, 1152-1161, https://doi.org/10.1039/TF9363201152, 1936.

Manninen, H. E., Nieminen, T., Asmi, E., Gagné, S., Häkkinen, S., Lehtipalo, K., Aalto, P., Vana, M., Mirme, A., Mirme, S., Hõrrak, U., Plass-Dülmer, C., Stange, G., Kiss, G., Hoffer, A., Törő, N., Moerman, M., Henzing, B., de Leeuw, G., Brinkenberg, M., Kouvarakis, G. N., Bougiatioti, A., Mihalopoulos, N., O'Dowd, C., Ceburnis, D., Arneth, A., Svenningsson, B., Swietlicki, E., Tarozzi, L., Decesari, S., Facchini, M. C., Birmili, W., Sonntag, A., Wiedensohler, A., Boulon, J., Sellegri, K., Laj, P., Gysel, M., Bukowiecki, N., Weingartner, E., Wehrle, G., Laaksonen, A., Hamed, A., Joutsensaari, J., Petäjä, T., Kerminen, V. M., and Kulmala, M.: EUCAARI ion spectrometer measurements at 12 European sites – analysis of new particle formation events, Atmospheric Chemistry and Physics, 10, 7907-7927, https://doi.org/10.5194/acp-10-7907-2010, 2010.

Petters, M. D., and Kreidenweis, S. M.: A single parameter representation of hygroscopic growth and cloud condensation nucleus activity, Atmospheric Chemistry and Physics, 7, 1961-1971, https://doi.org/10.5194/acp-7-1961-2007, 2007.

Pikridas, M., Vrekoussis, M., Sciare, J., Kleanthous, S., Vasiliadou, E., Kizas, C., Savvides, C., and Mihalopoulos, N.: Spatial and temporal (short and long-term) variability of submicron, fine and sub-10 µm particulate matter (PM1, PM2.5, PM10) in Cyprus, Atmospheric Environment, 191, 79-93, https://doi.org/10.1016/j.atmosenv.2018.07.048, 2018.